Radiation Energy Budget Studies Using Collocated AVHRR and ERBE Observations

STEVEN A. ACKERMAN

Cooperative Institute of Meteorological Satellite Studies, Department of Atmospheric and Oceanic Sciences, University of Wisconsin—Madison, Madison, Wisconsin

TOSHIRO INOUE

Meteorological Research Institute, Ibaraki, Japan

(Manuscript received 29 May 1993, in final form 22 July 1993)

ABSTRACT

Changes in the energy balance at the top of the atmosphere are specified as a function of atmospheric and surface properties using observations from the Advanced Very High Resolution Radiometer (AVHRR) and the Earth Radiation Budget Experiment (ERBE) scanner. By collocating the observations from the two instruments, flown on *NOAA-9*, the authors take advantage of the remote-sensing capabilities of each instrument. The AVHRR spectral channels were selected based on regions that are strongly transparent to clear sky conditions and are therefore useful for characterizing both surface and cloud-top conditions. The ERBE instruments make broadband observations that are important for climate studies. The approach of collocating these observations in time and space is used to study the radiative energy budget of three geographic regions: oceanic, savanna, and desert.

1. Introduction

Climate feedback mechanisms are often observed as changes in the radiation energy budget of the earth–atmosphere system. To fully comprehend the coupling between climate change and perturbations in the earth radiation budget (ERB), we must address the physical relationships between changing atmospheric and surface conditions, and resultant changes in the ERB. This is best achieved through analysis of Earth Radiation Budget Experiment (ERBE) data in conjunction with coincident observations of atmospheric constituents (e.g., clouds, water vapor, and temperatures) obtained from other instruments. Full advantage of the capabilities of each instrument for monitoring climate parameters is attained by collocating the observations in time and space. For example, the ERBE scanning radiometers were designed to monitor the top-of-the-atmosphere energy budget. These instruments were not designed to derived cloud climatologies or surface properties. The Advanced Very High Resolution Radiometer (AVHRR) is better suited for defining the surface characteristics and identifying clouds. There have been several recent studies that combined monthly mean ERBE observations with monthly means from independent sources (e.g., Raval and Ramanathan 1989; Stephens and Greenwald 1991). While such studies are extremely instructive, they do not improve on the inherent weakness of the individual instantaneous instrument measurement. Collocation of individual fields of view of the AVHRR and ERBE instruments was used by Li and Leighton (1991) to study the sensitivity of cloud radiative forcing in the Arctic to errors in scene identification resulting from using the ERBE instrument alone. Ackerman et al. (1992) used collocated AVHRR, High-Resolution Infrared Sounder (HIRS/2) and ERBE observations to study physical processes associated with the radiative energy budget at the top of the atmosphere. Baum et al. (1992) used collocated AVHRR and HIRS/2 observations to derive cloud optical properties.

The present study combines AVHRR and ERBE observations to investigate the sensitivity of fluxes at the top of the atmosphere to changing atmospheric and surface properties. By collocating these observations, cloud radiative forcing over a tropical ocean is described as a function of cloud type—stratus, cumulonimbus, and cirrus. For clear-sky ocean conditions, the greenhouse parameter, the ratio of the outgoing longwave flux at the top of the atmosphere, and the blackbody flux from the surface are composited as a function of the split-window temperature difference, which is an index of the total water vapor amount in the atmospheric column. Over western Africa, changes

Corresponding author address: Dr. Steven A. Ackerman, CIMSS, Space Science and Engineering Center, University of Wisconsin—Madison, 1255 West Dayton Street, Madison, WI 53706.

in the energy budget at the top of the atmosphere are described with respect to changes in surface properties.

Section 2 describes the instruments and observations used in the study, as well as the collocation procedure. Section 3 presents the results, which are then summarized in section 4.

2. Data analysis

This study utilizes AVHRR and ERBE observations made from the *NOAA-9* polar-orbiting satellite over the tropical eastern Pacific (approximately 10°S–20°N, 100°–140°W) and for western Africa (approximately 0°–25°N, 10°W–15°E) for the year 1986, for approximately 6 days per month. The *NOAA-9* nominal equator crossing times are 0900 and 2100 UTC.

The AVHRR makes measurements in five spectral bandpasses: channel 1 (0.56–0.68 μm); channel 2 (0.725–1.1 μm); channel 3 (3.55–3.93 μm); channel 4 (10.3–11.3 μm); and channel 5 (11.5–12.5 μm). These five channels are regions where atmospheric gases have weak absorption; data are therefore appropriate for studying surface properties, such as sea surface temperature and vegetation indexes, and cloud-top properties. Calibration of the AVHRR is discussed by Weinreb et al. (1990). Inoue (1987) developed a cloud-type classification based on the AVHRR observed equivalent brightness temperature in channel 4 (11 μm) and the temperature difference between channels 4 and 5 (11–12 μm). On the basis of the two-dimensional histogram of the 11-μm temperature and 11–12-μm temperature difference, cirrus, dense cirrus, cumulonimbus, cumulus, and stratus clouds can be classified over the ocean. This study uses this classification scheme—the split-window method—discussed in more detail below.

ERBE observes the broadband energy budget at the top of the atmosphere. The ERBE instrument package includes a scanning radiometer to measure the broadband shortwave (SW) and longwave (LW) radiances. The instrument, and its calibration, is discussed by Kopia (1986). Barkstrom et al. (1989) and Smith et al. (1986) described the method of inverting the instantaneous scanner observations for the top-of-atmosphere fluxes. These inversion procedures depend on scene identification to select appropriate spectral filter function correction, and anisotropic models. Wielicki and Green (1989) presented the ERBE method of scene identification, while Dieckman and Smith (1989) discussed errors in outgoing fluxes associated with scene misidentification.

To collocate the AVHRR pixels within the ERBE footprint requires knowledge of the scanning geometry of both instruments. The AVHRR scans by means of a mirror that makes a full revolution in 1/6 s and has a cross-track scan angle of ±55.4°, resulting in 2048 scenes in a scan line. The mirror step angle is approximately 0.0541°. The AVHRR instrument has a nominal spatial resolution of 1.1 km at nadir. The AVHRR data available in this study is global area coverage (GAC) data, derived by averaging four out of five pixel elements of every third line. The nominal resolution of GAC data is considered to be 4 km at nadir.

The ERBE instrument samples at a rate of 0.033 s while scanning the earth at a scan rate of 66.7° s^{-1}. The ERBE field stop is 3° × 4.5°; considering the point spread function of the ERBE scanner, the nadir field of view (FOV) is approximately 35 km. Because of the large ERBE FOV overlap, approximately 35% at nadir, AVHRR pixels are collocated within every other ERBE line and element. The cross-track scan angle is adjustable to allow along-track scanning for developing angular correction models; this paper considers the cross-track scan mode only. Given the scanning geometry of each instrument, the AVHRR pixels are collocated within the ERBE footprint following the algorithm outlined by Aoki (1980) for collocating AVHRR pixels within the HIRS/2 footprints. This geometric solution to collocation can be considered a close approximation; however, it may not be exact due to errors in the satellite position, curvature of the earth, and any changes in mirror angle and scan rate that occur while the satellite is in space. In addition, the ERBE pixel location latitude and longitude are defined at the top of the atmosphere (30 km) while the AVHRR pixel emphemeris data are defined at the surface. Such errors can be thought of as causing a shift in the relative position of the AVHRR imaged data with respect to an image of the ERBE data. To account for this slip, the AVHRR pixels are shifted along the track of the satellite and/or along the scan direction to minimize

$$\frac{1}{N}\sum_{l=1}^{N}[\bar{R}_A(l) - R_E(l)]^2,$$

where N is the number of collocated ERBE fields of view, $R_E(l)$ is the ERBE measurement, and $\bar{R}_A(l)$ is the mean AVHRR radiance. Best correlations occurred with shifts of 1 lines and 2 elements of the AVHRR image. Figure 1 is an example of this correlation for a single geographic region. The linear correlation coefficient between the ERBE and AVHRR measurements, for this particular scene, is greater than 0.98 for both the solar and infrared comparisons. This correlation (which is typically greater than 0.85) is often less than that of collocated AVHRR and HIRS/2 pixels (Ackerman et al. 1992; typically greater than 0.95) due to the different spectral bandpasses of the AVHRR and ERBE instruments.

3. Results

Results are presented for three geographic regions; oceanic, savanna, and desert. These three geographic

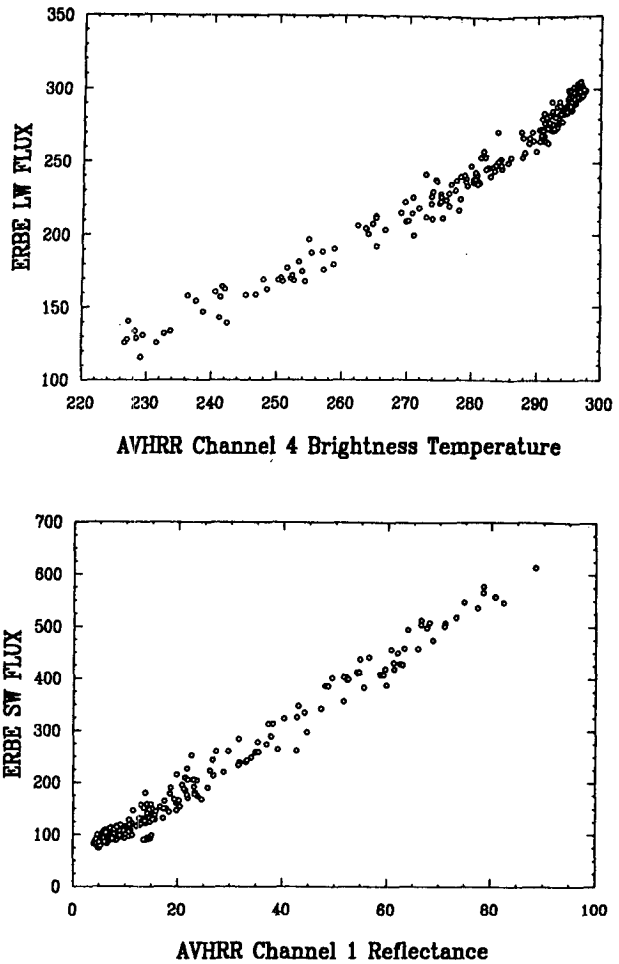

FIG. 1. Scatter diagram of ERBE footprint values and mean AVHRR pixels within the ERBE field of view. (a) AVHRR 11-μm temperature (K) and ERBE broadband longwave flux (W m^{-2}) and (b) AVHRR channel 1 reflectance (%) and ERBE broadband shortwave flux (W m^{-2}).

regions were selected because of the varying degrees to which the atmosphere and surface are coupled together. The radiative energy budget at the surface is coupled to the atmosphere for all surfaces, as the composition and temperature structure of the atmosphere determine the incoming fluxes at the surface. At the top of the atmosphere (TOA) the upwelling radiation may be decoupled from the surface fluxes due to the intervening atmosphere.

The atmosphere and surface are coupled over the ocean regions—atmospheric water vapor content is a function of the surface temperature (Stephens 1990). We therefore expect good correlations between clear-sky TOA fluxes and surface properties (e.g., sea surface temperature). An ocean region was also selected because the surface is uniform in temperature and albedo, particularly when compared to land, thus enabling us to use these combined observations to study the radiative impact of different cloud types.

The Sahel region chosen as feedback between the land surface and atmosphere may be a self-reinforcing mechanism of droughts (Charney 1975) in this region. Satellite observations provide a useful tool for monitoring the seasonal and annual weather of geographic regions where rains are highly variable, in both time and space, and the surface properties change markedly with precipitation, as in the Sahel. A disadvantage of satellite analysis is that satellites provide only "snapshots" of the present conditions and not physical links between mechanisms. Investigation of this link between the surface properties and the TOA energy budget is accomplished using the combined observations.

The final geographic locale considered was a desert region, the Sahara. With very little if any vegetation, the desert may at first seem a simple geographic region for developing energy budget parameterizations. The atmosphere is coupled to the surface via strong sensible heat fluxes, which can result in mixed-layer depths of 5 km in summer. We might therefore expect a coupling between the surface and the TOA fluxes. On the other hand, advection of atmospheric water vapor and dust storms tends to decouple the energy budget at the top of the atmosphere from the surface physical properties. The collocated observations demonstrate the complex nature of deserts.

a. Oceanic clear-sky results

The effect of water vapor on the planetary radiative energy budget over oceans has recently been described using satellite observations by Raval and Ramanathan (1989), Stephens and Greenwald (1991), and Ackerman et al. (1992). The greenhouse effect of water vapor is quantified based on the greenhouse parameter

$$G = \frac{T_s^4}{T_e^4},$$

where T_s is the sea surface temperature and T_e is the effective clear-sky planetary temperature determined from the ERBE-measured outgoing longwave radiation (OLR $= \sigma T_e^4$). While ERBE incorporates a scene identification algorithm, the present study determines clear-sky scenes based on the split-window technique (Inoue 1987), in conjunction with the uniformity of the AVHRR brightness temperature within the ERBE footprint. Specifically, a clear-sky ocean scene is defined if the 11-μm brightness temperature (BT_{11}) is greater than 280 K, the BT difference between 11 and 12 μm (ΔBT_{11-12}) is $0 \leq \Delta BT_{11-12} \leq 3$, and the standard deviation of the BT_{11} within the ERBE footprint is less than 0.1 K. This last condition is referred to as the scene uniformity and is calculated using radiance observations. Under clear sky conditions, sea surface temperatures are derived from AVHRR observations

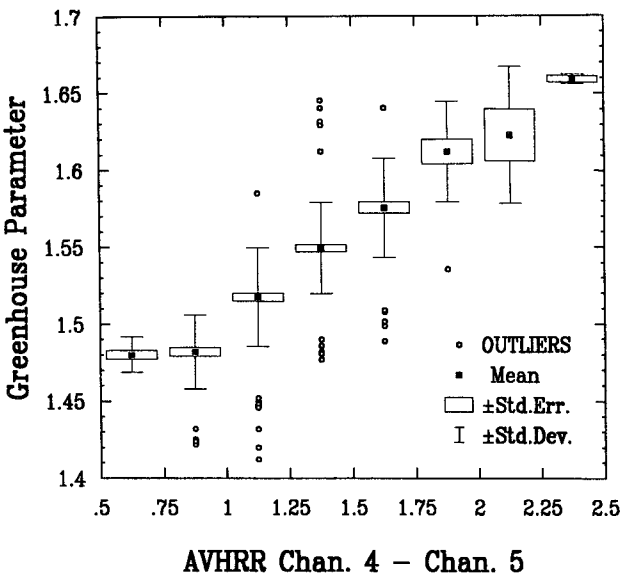

FIG. 2. AVHRR split-window difference (K) versus the greenhouse parameter. Solid boxes represent the mean relationship, open boxes are the standard error, and the vertical bars are the standard deviation.

using the NOAA (National Oceanic and Atmospheric Administration) operational method described by McClain (1989).

Previous studies (e.g., Raval and Ramanathan 1989; Stephens and Greenwald 1991; Ackerman et al. 1992) have demonstrated a dependence of the greenhouse parameter on sea surface temperature. This relationship is driven by the coupling between sea surface temperature and precipitable water; a relationship recently discussed by Stephens (1990). The ΔBT_{11-12} is an indication of the atmospheric water vapor structure in the lower atmosphere, which makes a large contribution to the total precipitable water. The relationship derived in the present study is shown in Fig. 2 as a box–whisker diagram. This figure was generated by compositing the observed G over a 0.25° interval of ΔBT_{11-12} for the entire dataset. The solid box represents the mean over the interval, the open rectangle the standard error, and the vertical lines the standard deviation. The open circles labeled outliers are observations that fell below or above the mean by more than two standard deviations. This figure demonstrates the relationship between the greenhouse parameter and ΔBT_{11-12}, showing a dependence between the greenhouse parameter and ΔBT_{11-12} between 1° and 2°. Stephens and Greenwald (1991) demonstrated the dependence of G on total precipitable water. As the split-window difference is related to the total precipitable water, Fig. 2 is in agreement with the previous studies. A linear fit of G with the split window explains 60% of the variance and has a correlation coefficient of 0.77. The variability about the linear relationship is due likely to variations in the upper-tropospheric water vapor (Ackerman et al. 1992; Stephens and Greenwald 1991). The relationship between G and ΔBT_{11-12} for $1° > \Delta BT_{11-12}$ for $1° > \Delta BT_{11-12} > 2°$ is difficult to state due to the small sample, as indicated in the frequency-of-occurrence diagram shown in Fig. 3. This histogram also indicates a seasonal variation in temperature differences associated with the seasonal variation in precipitable water.

b. *Oceanic cloudy-sky results*

The radiative properties of clouds are described in terms of cloud radiative forcing defined as the difference between the observed flux and the clear-sky flux: for the longwave,

$$\mathrm{LWCF} = \mathrm{OLR}_{\mathrm{clr}} - \mathrm{OLR}_{\mathrm{cld}},$$

where OLR is the outgoing longwave radiation and the subscripts clr and cld represent clear and cloudy conditions; for the shortwave,

$$\mathrm{SWCF} = S_0(\alpha_{\mathrm{clr}} - \alpha_{\mathrm{cld}}),$$

where S_0 is the incoming solar radiation and α is the observed albedo. Ramanathan et al. (1989) and Harrison et al. (1990) derived the global distribution of cloud forcing based on ERBE observations on a spatial scale of 2.5° × 2.5° and monthly averages. Ackerman et al. (1992) combined ERBE, AVHRR, and HIRS/2 observations to describe cloud forcing as a function of cloud amount and altitude. Due to the similar size in the ERBE and HIRS/2 fields of view, Ackerman et al. (1992) described these relations on a spatial scale of 3 × 3 ERBE footprints. The advantage of this study is

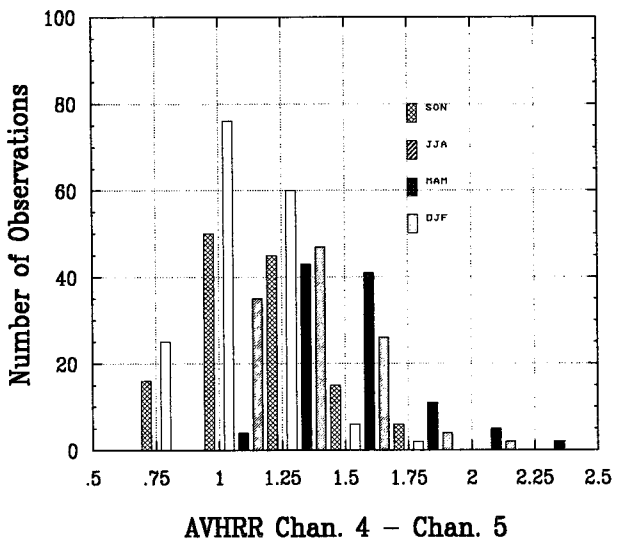

FIG. 3. Histogram of the split-window difference (K) as a function of season for a region in the eastern Pacific.

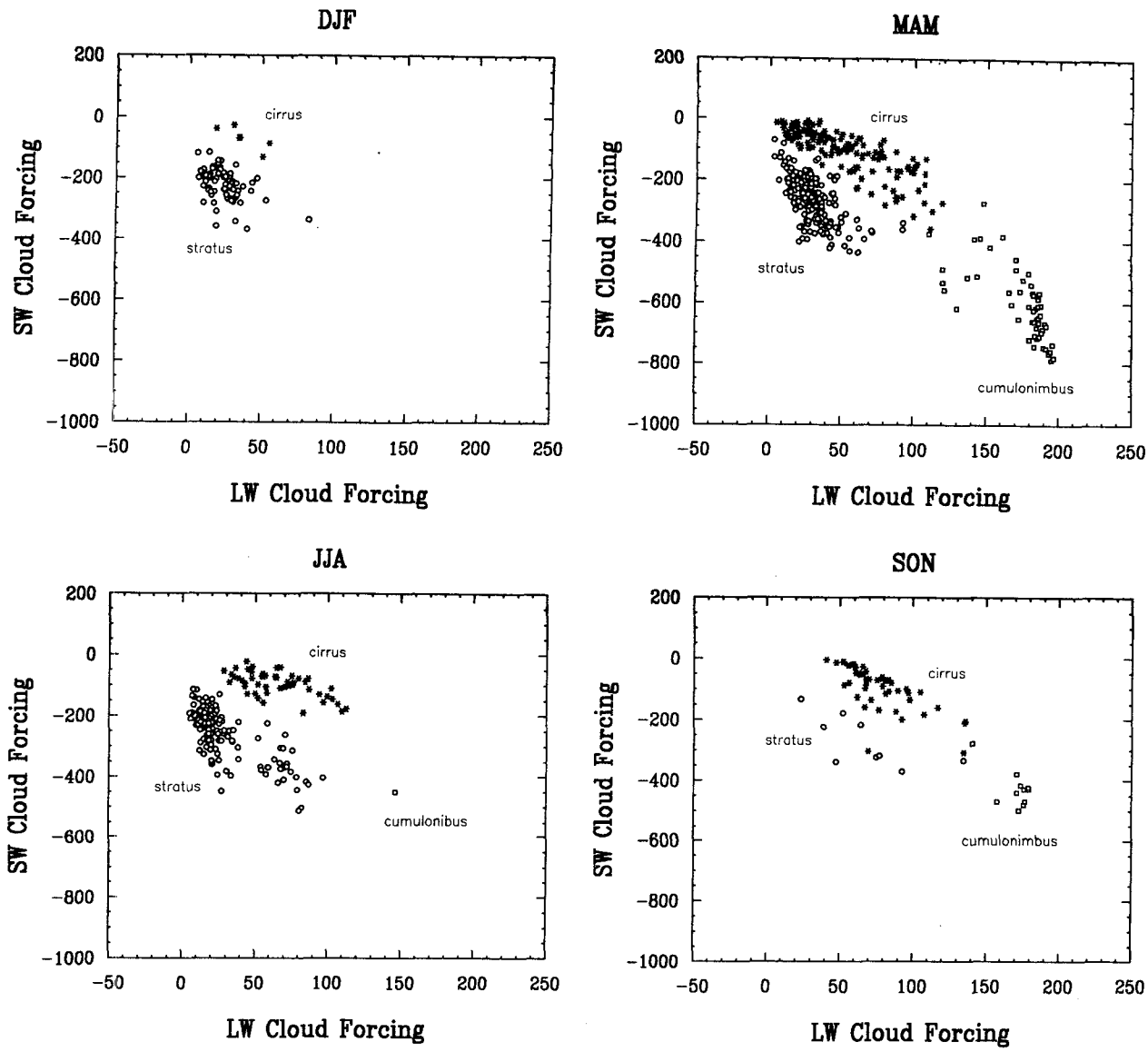

FIG. 4. The longwave and shortwave cloud forcing (W m^{-2}) as a function of season for different cloud classifications: circles—stratus; stars—cirrus; boxes—cumulonimbus.

the higher spatial resolution, the use of individual ERBE footprints, and a classification of cloud type. Li and Leighton (1991) combined AVHRR and ERBE observations to study cloud radiative forcing in the Arctic. The current study uses a different collocation procedure and different scene identification approach and addresses the tropical regions.

The split-window technique developed by Inoue (1987, 1989) is based on a threshold technique applied to a two-dimensional histogram of the brightness temperature of the 11-μm channel and the brightness temperature difference between the split-window observations. In this study the ΔBT threshold for low-level clouds is $\Delta BT < 1.0°$; the BT_{11} is between 250 and 294 K. Cumulonimbus clouds are identified when the BT_{11} is less than 250 and the ΔBT is less than 1.5° and greater than −2°. The final category is cirrus, in which the BT_{11} is less than 294° and the ΔBT ranges between 3° and 9°.

Radiative cloud forcing is shown in Fig. 4, composited as a function of season. Clear-sky values were determined for each month as discussed above. The three cloud classifications are stratus, cirrus, and cumulonimbus. The cumulonimbi display the largest SWCF and LWCF. Notice that stratus clouds and thin cirrus clouds can have the same effect on modifying the clear-

sky OLR; however, the stratus has a larger effect on the shortwave because the water contents of stratus are generally larger than the ice content of cirrus. These types of relationships are difficult to derive directly with ERBE observations alone. A similar relationship between the LWCF and SWCF with respect to cloud type exists for each of the seasons. The analysis as a function of season clearly indicates an annual variation in cloud type. Cumulonimbus clouds were generally not observed in the summer and winter seasons and were at a maximum in the spring. Low-level clouds are observed throughout the year as would be expected over the oceans. Thus, seasonal changes in cloud forcing for this region are likely due to changes in cloud-type distribution.

c. *Semidesert clear-sky results*

The previous sections combined the two observations to investigate the relationship between outgoing longwave radiation at the TOA and the brightness temperature difference between spectral observations at 11 and 12 μm. This relationship comes about because of the dependence of the observations on atmospheric water vapor content, which is strongly tied to sea surface temperature. The next step is to investigate relationships between TOA radiative fluxes and surface characteristics over land. An important component of the ERBE program has been its observation of cloud forcing, which is regionally dependent (Harrison et al. 1990). Changes in cloud forcing can result from changes in cloud amount or type, atmospheric condition, or surface properties. The effect of changing cloud type over oceans was demonstrated in the previous section. To understand cloud forcing over land we need to address coupling between the surface and the TOA energy budget. A classic example of this coupling is the desertification proposed by Charney (1975). This section is a first attempt at addressing these issues from combined AVHRR and ERBE satellite observations.

As in the previous section, the AVHRR pixels are collocated within the ERBE footprint. Shortwave and longwave fluxes at the TOA are specified from the ERBE observations. Surface vegetation characteristics and temperature are estimated using the AVHRR observations. The surface properties are expressed in terms of the normalized difference vegetation index (NDVI), derived from the AVHRR channel 1 and channel 2 observations (Tucker et al. 1984):

$$\mathrm{NDVI} = \frac{\mathrm{Chan\ 2} - \mathrm{Chan\ 1}}{\mathrm{Chan\ 2} + \mathrm{Chan\ 1}}.$$

The NDVI is a function of greenness and amount of vegetation with the higher values associated with greener scenes (Tucker et al. 1984; Justice et al. 1985; Townshend and Justice 1986; Tucker et al. 1986). In addition, the AVHRR data are used to determine the cloud- and dust-free regions as well as the scene homogeneity within the ERBE footprint. Dust storms are indicated by negative brightness temperature differences between the 11- and 12-μm channels (Ackerman and Chung 1992). Results are presented for 6 days in October 1986 for the Sahel region.

The box–whisker diagram (Fig. 5) is used to depict the relationship between surface NDVI and TOA fluxes for the Sahel region between 5° and 15°N. Points different from the mean by more than ±2 standard deviations are plotted as outliers. The vegetation of this semiarid region is primarily grasses. As the surface NDVI decreases, due to either less vegetation or drying vegetation, the albedo increases (Fig. 5a). A second-order polynomial fit of the albedo versus the NDVI explains 66% of the variance ν with a correlation r of 0.82. The OLR (Fig. 5b) also displays a tendency to increase as the NDVI decreases (ν = 54%, r = 0.73). Some of the variability depicted in Fig. 5 results from atmospheric variability, as well as instrument characteristics. For clear sky conditions, the ERBE-measured longwave flux is more sensitive to the state of the atmosphere than the albedo and NDVI, which accounts for the smaller correlation with NDVI. The coupling of the albedo and OLR to surface characteristics, as indicated by their respective relationships with NDVI, results in the relationship depicted in Fig. 6 (r = 0.61). For this region of western Africa, when the albedo increases, the LW flux at the TOA correspondingly increases, in agreement with the desertification mechanism of Charney.

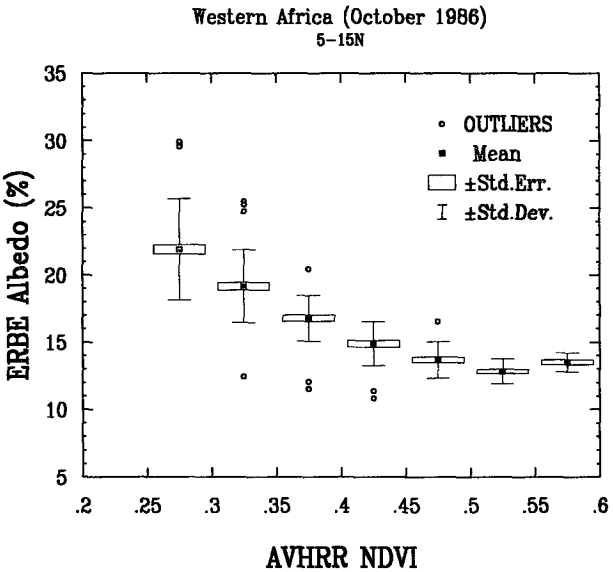

FIG. 5a. Box–whisker diagram of AVHRR NDVI versus ERBE albedo (%) for the Sahel region.

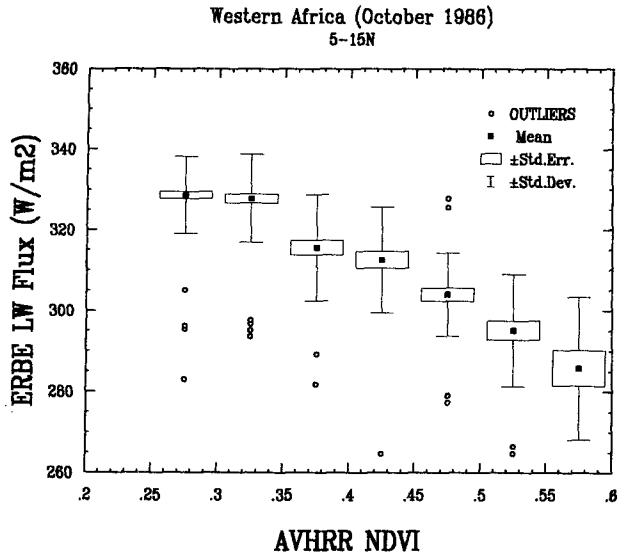

FIG. 5b. Box–whisker diagram of AVHRR NDVI versus ERBE outgoing longwave flux (W m^{-2}) for the Sahel region.

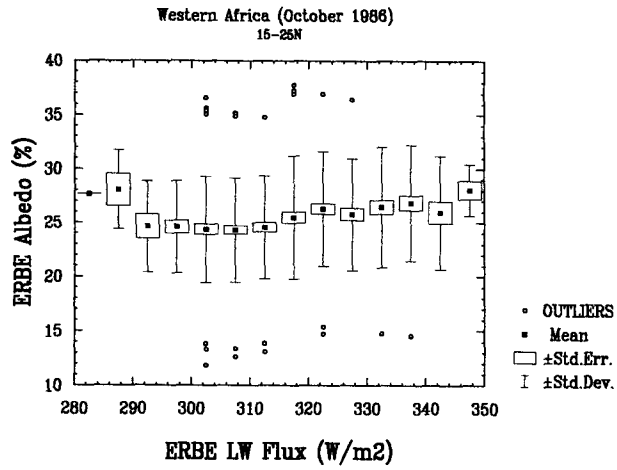

FIG. 7. Box–whisker diagram of ERBE OLR (W m^{-2}) versus ERBE albedo (%) for the interior desert region.

d. Desert clear-sky results

We now address the relationships for a geographic region denude of vegetation at 15°–25°N. The NDVIs for soil range between 0.2 and 0.3. As the NDVI is not related to soil type, there is no relationship between NDVI and the TOA fluxes for this region. One might expect a relationship between the albedo and OLR, such that as the surface gets darker, the albedo gets lower, with the OLR increasing due to an increased surface temperature. Analysis of the ERBE-measured albedo and OLR is depicted in Fig. 7, suggesting little correlation ($r = 0.15$). This spectral decoupling may result from different spectral characteristics of the atmosphere, which are more transparent to the SW than the LW. The OLR and broadband albedo are correlated with the AVHRR 11-μm brightness temperature and channel 1 reflectance, respectively, indicating the importance of the surface in determining the magnitude of TOA fluxes. An analysis of the AVHRR 11-μm brightness temperature and AVHRR visible reflectance (Fig. 8) is similar to broadband results in that no correlations are apparent. Thus, the variance between TOA broadband fluxes (Fig. 7) is not due solely to atmospheric variability; surface characteristics also play

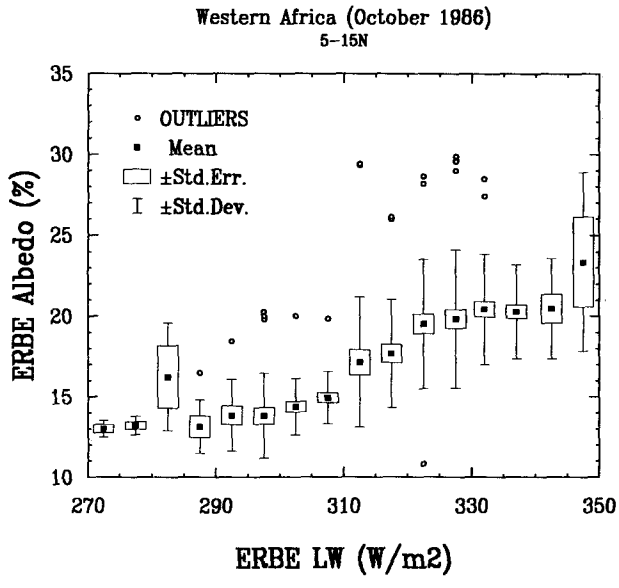

FIG. 6. Box–whisker diagram of ERBE OLR (W m^{-2}) and albedo (%) for the Sahel region.

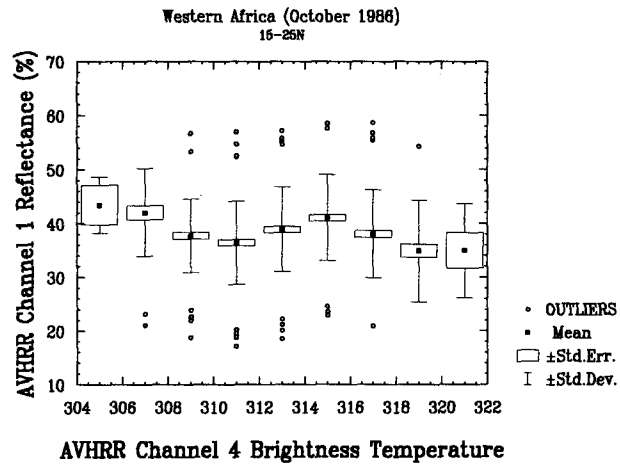

FIG. 8. Box–whisker diagram of AVHRR 11-μm brightness temperature (K) versus the AVHRR visible channel reflectance (%) for the interior desert region.

an important role. For example, different soil types with the same albedo may have different specific heats—for the same amount of absorbed solar energy, one soil may raise its temperature faster than another, thereby decoupling the SW properties from the LW.

The present analysis indicates that the TOA fluxes are not decoupled from the surface properties; rather, it appears that for the region as a whole, the TOA fluxes and surface properties are decoupled spectrally. It may also be that the signal we are seeking is weak and therefore requires suitable time and space averaging to become apparent. Observations (e.g., Smith 1986) have demonstrated that the mean properties of the desert surface are controlled by radiative exchanges at the surface. What this study suggests is that parameterizations derived for one geographic region may not be easily extended to another desert region.

4. Summary

An approach to studying the radiative energy budget of the planet using collocated AVHRR and ERBE observations is presented. By collocating the observations from the two instruments flown on the *NOAA-9* and *NOAA-10* satellites one is able to take advantage of the remote-sensing capabilities of each instrument. The AVHRR spectral channels were selected based on regions that are weakly absorbing and are therefore useful for characterizing surface and cloud-top conditions. The ERBE instruments make broadband observations that are important for climate studies. By combining the observations, we address how changing surface and cloud conditions affect the energy budget at the top of the atmosphere. The disadvantage of the technique is that observed relationships between the surface and cloud properties and TOA fluxes are inherently noisy. The analysis therefore requires many collocated observations or appropriate statistical representation of the data.

The results can be summarized as the following:

- The greenhouse parameter is well correlated with the split-window brightness temperature difference of the AVHRR (a linear fit of G with ΔBT_{11-12} explains 60% of the variance with a correlation coefficient of 0.77). For clear sky conditions, the split-window difference is an indication of the water vapor loading, and the results are therefore consistent with previous studies.
- The collocated observations were used to derive cloud radiative forcing as a function of three cloud types—cumulonimbus, stratus, and cirrus. Cloud types classified by the split-window technique show reasonable relationships with the TOA fluxes observed by ERBE. Of the three cloud types, cumulonimbi have the largest effect in modifying the clear-sky SW and LW fluxes. Stratus clouds have a larger SW cloud forcing than cirrus, although LW cloud forcing for the two cloud types show similar values. While no surprises were found in the analysis, the approach can be extended to analyze the effect of cloud microphysical properties, as derived from the AVHRR observations, on the top-of-the-atmosphere energy budget as measured by ERBE.
- There appears to be a good correlation between vegetation cover, in terms of the AVHRR NDVI product, and ERBE top-of-the-atmosphere fluxes for the Sahel region. A second-order polynomial fit to the ERBE albedo and AVHRR NDVI observations explains 66% of the variance with a correlation coefficient of 0.87. A similar least-squares fit to the AVHRR NDVI and collocated ERBE LW flux yields a correlation of 0.73, which explains 54% of the variance. The weaker correlation between ERBE LW flux and NDVI is attributed to atmospheric variability. The observed relationship supports the land–atmosphere feedback mechanism whereby land surface changes can induce changes in the radiative energy balance that could support further changes at the surface. The observed relationships may be useful in verifying land surface feedback mechanisms of general circulation models.
- No apparent relationship between the SW and LW fluxes exists in the interior Sahara desert indicating, from an energy balance perspective, the complex nature of deserts. The analysis suggests that radiative parameterizations derived for one desert region may not be easily extended to another desert region due to differences in soil characteristics.

Acknowledgments. This work was supported by NASA under Grant NAS1-18272. We are indebted to the programming efforts of Richard A. Frey.

REFERENCES

Ackerman, S. A., and H. Chung, 1992: Radiative effects of airborne dust on regional energy budgets at the top of the atmosphere. *J. Appl. Meteor.*, **31**, 223–233.

——, R. A. Frey, and W. L. Smith, 1992: Radiation budget studies using collocated observations from AVHRR, HIRS/2 and ERBE instruments. *J. Geophys. Res.*, **97**, 11 513–11 525.

Aoki, T. A., 1980: A method for matching the HIRS/2 and AVHRR pictures of TIROS-N satellites. Tech. Note 2, Meteorological Satellite Center, Japan, 15–16.

Barkstrom, B. R., E. F., Harrison, G. Smith, R. Green, J. Kebler, R. Cess, and the ERBE Science Team, 1989: Earth Radiation Budget Experiment (ERBE) archival and April 1985 results. *Bull. Amer. Meteor. Soc.*, **70**, 1254–1262.

Baum, B. A., B. A. Wielicki, P. Minnis, and L. Parker, 1992: Cloud property retrieval using merged HIRS and AVHRR data. *J. Appl. Meteor.*, **31**, 351–369.

Charney, J., 1975: Dynamics of deserts and drought in the Sahael. *Quart. J. Roy. Meteor. Soc.*, **101**, 193–202.

Diekmann, F. J., and G. L. Smith, 1989: Investigation of scene identification algorithms for radiation budget measurements. *J. Geophys. Res.*, **94**, 3395–3412.

Harrison, E. F., P. Minnis, B. R. Barkstrom, V. Ramanathan, R. D. Cess, and G. G. Gibson, 1990: Seasonal variation of cloud radiative forcing derived from the earth radiation budget experiment. *J. Geophys. Res.*, **95**, 18 687–18 703.

Inoue, T., 1987: An instantaneous delineation of convective rainfall areas using split window data of *NOAA-7* AVHRR. *J. Meteor. Soc. Japan,* **65,** 469–480.

——, 1989: Features of clouds over the tropical Pacific during Northern Hemispheric winter derived from split window measurements. *J. Meteor. Soc. Japan,* **67,** 621–637.

Justice, C. O., J. R. G. Townshend, B. N. Holben, and C. J. Tucker, 1985: Analysis of the phonology of global vegetation using meteorological satellite data. *Int. J. Remote Sens.,* **6,** 1271–1318.

Kopia, L. P., 1986: Earth radiation budget experiment scanner instruments. *J. Geophys. Res.,* **24,** 400–406.

Li, Z., and H. G. Leighton, 1991: Scene identification and its effect on cloud radiative forcing in the Arctic. *J. Geophys. Res.,* **96,** 9175–9188.

McClain, E. P., 1989: Global sea surface temperatures and cloud clearing for aerosol optical depth estimates. *Int. J. Remote Sens.,* **10,** 763–769.

Ramanathan, V., R. D. Cess, E. F. Harrison, P. Minnis, B. R. Barkstrom, E. Ahmad, and D. Hartmann, 1989: Cloud-radiative forcing and climate: Results from the Earth Radiation Budget Experiment. *Science,* **243,** 57–63.

Raval, A., and V. Ramanathan, 1989: Observation determination of the greenhouse effect. *Nature,* **342,** 758–761.

Smith, E. A., 1986: The structure of the Arabian heat low. Part I: Surface energy budget. *Mon. Wea. Rev.,* **114,** 1068–1083.

Smith, G. L., R. N. Green, E. Raschke, L. B. Avis, J. T. Suttles, B. A. Wielicki, and R. Davies, 1986: Inversion methods for satellite studies of the earth's radiation budget: Development of algorithms for the ERBE mission. *Rev. Geophys.,* **24,** 407–421.

Stephens, G. L., 1990: On the relations between water vapor over the oceans and sea surface temperature. *J. Climate* **3,** 634–645.

——, and T. J. Greenwald, 1991: The earth's radiation budget and its relation to atmospheric hydrology. Part I: Observations of the clear sky greenhouse effect, *J. Geophys. Res.* **96,** 15 311–15 324.

Townshend, J. R. G., and C. O. Justice, 1986: Analysis of the dynamics of African vegetation using the normalized difference vegetation index. *Int. J. Remote Sens.,* **7,** 1435–1445.

Tucker, C. J., Gatlin, A., and S. R. Schneider, 1984: Monitoring vegetation in the Nile delta with *NOAA-6* and *NOAA-7* AVHRR. *Photogramm. Eng. Remote Sens.,* **50,** 53–60.

——, C. O. Justice, and S. D. Prince, 1986: Monitoring the grasslands of the Sahel 1984–1985. *Int. J. Remote Sens.,* **7,** 1571–1581.

Weinreb, M. P., H. E. Fleming, L. M. McMillin, and A. C. Neven-dorffer, 1981: Transmittance for the TIROS operational sounder. NOAA Tech. Rep. NESS85, U.S. Department of Commerce.

Wielicki, B. A., and R. N. Green, 1989: Cloud identification for ERBE radiative flux retrieval. *J. Appl. Meteor.,* **28,** 1133–1146.